J Mater Sci: Mater Med (2011) 22:2617–2629
DOI 10.1007/s10856-011-4447-8

Automated quantitative characterization of alginate/hydroxyapatite bone tissue engineering scaffolds by means of micro-CT image analysis

Francesco Brun · Gianluca Turco · Agostino Accardo · Sergio Paoletti

Received: 12 April 2011 / Accepted: 13 June 2011 / Published online: 18 September 2011

Abstract Accurate image acquisition techniques and analysis protocols for a reliable characterization of tissue engineering scaffolds are yet to be well defined. To this aim, the most promising imaging technique seems to be the X-ray computed microtomography (μ-CT). However critical issues of the analysis process deal with the representativeness of the selected Volume of Interest (VOI) and, most significantly, its segmentation. This article presents an image analysis protocol that computes a set of quantitative descriptors suitable for characterizing the morphology and the micro-architecture of alginate/hydroxyapatite bone tissue engineering scaffolds. Considering different VOIs extracted from different μ-CT datasets, an automated segmentation technique is suggested and compared against a manual segmentation. Variable sizes of VOIs are also considered in order to assess their representativeness. The resulting image analysis protocol is reproducible, parameter-free and it automatically provides accurate quantitative information in addition to the simple qualitative observation of the acquired images.

F. Brun (✉) · A. Accardo
Department of Industrial Engineering and Information Technology, University of Trieste, Via A. Valerio, 10, 34127 Trieste, Italy
e-mail: francesco.brun@phd.units.it

F. Brun
Sincrotrone Trieste S.C.p.A, Trieste, Italy

G. Turco · S. Paoletti
Department of Life Sciences, University of Trieste, Trieste, Italy

1 Introduction

Approaches in scaffold design must be able to create porous structures to attain desired mechanical function as well as mass transport properties. Material chemistry and the micro-architecture determine the functional properties of a scaffold as well as how cells interact with it [12]. In particular, for bone tissue engineering, osteoconductivity largely depends upon the geometry of the scaffold. The degree of porosity and interconnection of the pores are also crucial for the in vivo bone tissue ingrowth in terms of blood vessels invasion, migration and proliferation of osteoblasts and matrix deposition in the void spaces. Therefore, critical issues for the design of a scaffold concern pore size, pore geometry, spatial distribution of pores and their interconnections in order to correctly derive mechanical and mass-transport properties and improve the effectiveness of biomaterials for bone tissue engineering [36]. However, assessing these structural properties is a challenging task. While it seems obvious that a scaffold needs to have pores and channels to allow cells to grow within it with the proper supply of nutrients, it is not so obvious to determine a priori what their shape, dimensions and interconnections should be as well as how these parameters can be effectively assessed [18].

Commonly, two-dimensional (2D) imaging systems such as scanning electron microscopy (SEM) are used for these determinations [26], although 2D systems show limits for the evaluation of some scaffold characteristics such as pore interconnectivity. To this aim, the most promising technique seems to be the computed microtomography (μ-CT) [11] widely used for the characterization of scaffolds [4, 21, 27, 36, 43]. Micro-CT allows 3D images to be obtained of the internal core of a sample in a non destructive way and with a spatial resolution in the

micro-meter scale suitable for further quantitative analysis. However, accurate image analysis protocols able to extract quantitative measures and indices directly from μ-CT images are yet to be well defined.

The challenging part of the quantitative analysis of μ-CT images lies in segmentation, i.e., a voxel classification process in which an image is separated into subsets by assigning individual voxels to classes [40]. Micro-CT images are usually segmented by thresholding gray levels and the preferred choice of selecting the threshold value is mainly based on manual visual assessment [5–7, 14, 21]. However, such a process is subjective, time-consuming and factors like room lighting, monitor brightness/contrast settings, operator fatigue and limited gray-scale shade perception can affect the reproducibility of visual thresholding [38]. Therefore it is worthy to investigate alternative objective and automatic thresholding techniques in order to overcome the subjectivity of manual thresholding.

Jones et al. [15] proposed an edge-based kriging segmentation algorithm [32] which however involves the manual choice of two cutoff values. Likewise, the curve integration method proposed in [9, 10] first requires a manual assignment to train the process. Moore et al. [29] suggest to accept as the threshold the one producing a binary image in which the resulting porosity (percentage of background voxels over the total number) is similar to either the theoretical porosity (based on known porogen concentration) or to the measured porosity (based on mercury intrusion porosimetry). However, this technique clearly requires external data (the theoretical or measured porosity) for the segmentation.

In the present article, an effective image analysis protocol with a fully automatic segmentation is presented. Different automatic thresholding techniques are examined and quantitatively compared against a manual thresholding performed onto three different μ-CT datasets of alginate/hydroxyapatite composite scaffolds (Fig. 1). After the comparison, the thresholding technique resulting as the best one was selected to be part of the proposed automated protocol. Several quantitative descriptors are then selected as relevant and applied to both the manually and automatically segmented images in order to evaluate the differences between the proposed method and the results of a manual segmentation. Different Volumes Of Interest (VOIs) with variable size and position are also considered in order to assess the representativeness of the chosen VOIs, which is an important issue for the accuracy of the results. The considered alginate/hydroxyapatite scaffolds have been already characterized from a chemical and mechanical point of view in [43] and a few morphological descriptors were also extracted. In the present article, several quantitative descriptors are computed directly from μ-CT images without any particular assumption on the structure under investigation, i.e., the scaffold is considered as a generic two-phase micro-structure having an interconnected porous space. This more comprehensive and model-independent quantitative characterization combined with automatic segmentation and VOI representativeness considerations may fruitfully help the design and the analysis of bone tissue engineering scaffolds.

2 Materials and methods

2.1 Materials description

Sodium alginate (Alg) samples isolated from *Laminaria hyperborea* stipe were provided by FMC Biopolymer (Norway) (MW = $1.3\text{x}10^5$, FG = 0.69; FGG = 0.56, where G stands for the guluronic acid co-monomer, and FG and FGG for the total fraction of G units and GG diads, respectively). Hydroxyapatite powder (HApF) with granules of an average value of about 150 nm was from Fluka (USA). Preparation of nano-hydroxyapatite (nHAp) with average dimension of 120 nm was achieved following the indications reported elsewhere [30]. Three composite scaffolds were prepared as described in [43]: pure alginate gels (hydroxyapatite-free) prepared by replacing the hydroxyapatite with $CaCO_3$ (corresponding to 30 mM of Ca^{2+}) hereafter referred as Alg/$CaCO_3$, an alginate with hydroxyapatite powder from Fluka (hereafter Alg/HApF) sample and a alginate with nano-hydroxyapatite (Alg/nHAp) sample.

2.2 X-ray micro-CT imaging

The μ-CT images of the samples were acquired using a microfocus X-ray source in a cone beam geometry at the TOMOLAB station (www.elettra.trieste.it/Labs/TOMOLAB). All the μ-CT scans were performed with the following parameters: distance source-sample = 100 mm; distance source-detector = 400 mm; 1440 tomographic projections over a 360° scan angle; tube voltage = 40 kV; tube current = 200 μA; exposure time = 2.6 s; focal spot size = 5 μm; resulting spatial resolution = 6.25 μm. While the μ-CT setup is the same for all the samples, independent conversion of the images to 8-bit format was performed according to an automatic min/max normalization procedure. Doing so, the three μ-CT datasets have to be considered as independent and therefore the three gray-level scales are not comparable.

2.3 Volume of interest (VOI) extraction

The first step of image analysis consists in the extraction of one or more Volumes of Interest (VOIs). Roughly, the

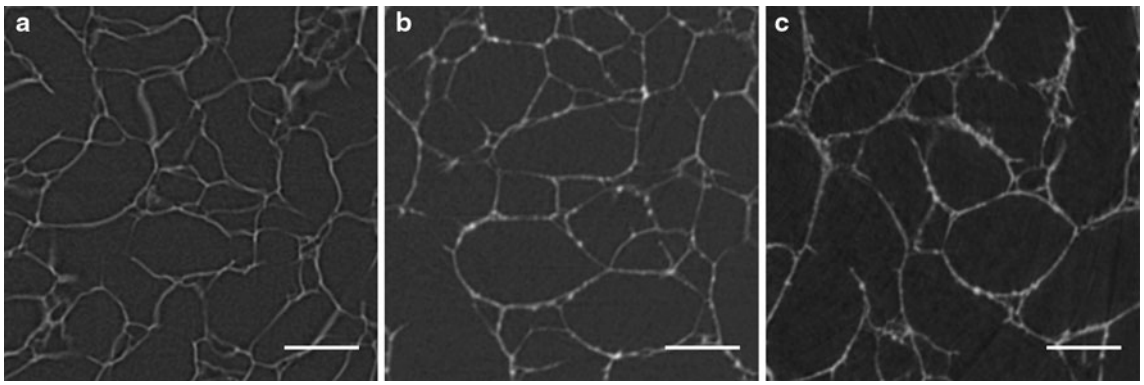

Fig. 1 A 2.5 × 2.5 mm^2 (400^2 pixels) slice of each considered micro-CT dataset: **a** Alg/$CaCO_3$; **b** Alg/nHAp; **c** Alg/HapF. The *scale bar* is 0.5 mm in all the images

extracted VOI should be small enough to be easily handled by the available computer hardware but at the same time it should be large enough to comprehend all the representative features of the sample. A common rule suggests to select VOIs having size of about one order of magnitude larger than the characteristic size of the underlying structure. This concept is sometimes referred to as macroscopic homogenization [33] but it requires some a priori knowledge about the underlying structure. In this study, four VOIs of 2.5 × 2.5 × 2.5 mm^3 (400^3 voxels) were extracted from each considered μ-CT dataset. This particular VOI size was chosen because it ensures to select four VOIs without no overlapped areas. Selecting an equal number of non-overlapped VOIs was observed to be difficult for increased sizes. The consideration of different VOIs allows to search for a dependence from the size of the VOI itself or from the area of the μ-CT dataset from which the VOI is extracted, i.e., how the investigated parameters behave when the size of the VOI is kept constant but its position is altered. However, more accurate considerations about the size of the VOI need to be performed in order to evaluate its representativeness and in this article a simple validation process is suggested. Each VOI was reduced in turn to 350^3, 300^3, 250^3, 200^3, 150^3 and 100^3 voxels (i.e., 2.2^3, 1.9^3, 1.6^3, 1.3^3, 0.9^3, 0.6^3 mm^3) by cropping an equal amount of voxels from each side and the cropped VOI was re-subjected to the analysis. The adoption of cropped versions from the original VOI instead of simply considering other resized VOIs simplify the computational requirements of this validation process and does not require user's involvement for the selection of the smaller VOIs.

2.4 Automated image thresholding

After VOI extraction, a segmentation process is required. Several automatic thresholding techniques have been proposed in the literature [41]. In the present article, seven automatic fixed-threshold techniques are taken into account. In principle, a global threshold for the whole 3D dataset is preferable and this is coherent with the typical behavior of a human operator inspecting all the reconstructed stack of images. However, in this study each VOI was subjected to the automatic segmentation techniques. This allows to check for the robustness of the automatic thresholding methods to be checked, i.e., how much the methods are affected by small histogram variations resulting from different VOIs extracted from different areas of the μ-CT dataset.

Next, the automatic thresholding techniques considered in the present study are briefly summarized. Kittler and Illingworth [20] proposed a method that consists in arbitrarily dividing the histogram into two parts (the foreground and the background), modeling each part with a normal distribution, comparing the resulting model based on a mixture of these normal distribution with the original histogram and assuming as optimal the threshold that minimizes a criterion function based on the classification error probability. Ridler and Calvard [39] advanced a method in which a unique threshold is assumed to be the average of the foreground and background class means. The means of the two parts can be evaluated only after the threshold is determined, but the threshold needs to be computed from the two means. Therefore, an iterative algorithm was suggested: first, an initial threshold is selected (the mean of the entire histogram is a sufficient starting point), then the two means for the two distributions on either side of the threshold are calculated. A new threshold is obtained by averaging these means and the process continues until the value of the threshold converges. Otsu [34] suggested to compute the intra-class variance, i.e., the weighted sum of the variances of each class (the background and the foreground) adopting the number of voxels in the class as a weight. Among all the possible thresholds, the optimal is the one that minimizes this intra-class variance. The Tsai's [42] method first computes gray-level moments from the input's histogram, and then obtains the threshold according to the principle

that gray-level moments keep unchanged before and after thresholding. The Pun's [37] method is based on entropic thresholding: an entropy-thresholded image is the one that preserves (as much as possible) the information contained in the original unthresholded image in terms of entropy. Kapur et al. [16] improved the Pun's approach considering the image foreground and background as two different classes of events. It first measures the class entropies, which is interpreted as a measure of class compactness. When the sum of the two class entropies reaches its maximum, the image is said to be optimally thresholded. Finally, Rajagopalan et al. [38] proposed an automatic thresholding method which exploits the feature-localizing characteristics of Fourier phases. For each possible threshold, the phase image of the thresholded image is computed and compared against the phase image of the original gray-level image. The best threshold is the one for which the normalized cross correlation of the phase images is maximum.

In the presently proposed protocol the segmentation process includes a parameter-free post-thresholding step as an attempt to reduce misclassified voxels. Since a scaffold possesses an interconnected porous network, an easy way to perform an effective post-thresholding "cleaning" could be obtained by simply removing internal connected components, i.e. connected components that do not "touch" VOI margins. This filter is included into the proposed segmentation process as a post-thresholding step (see Fig. 2). An example of the results of the whole segmentation process (thresholding and post-processing) is reported in Fig. 3.

In order to test the reliability (or the failure) of an automatic thresholding [46], in the present article the automatically segmented images obtained according to the automatic methods are compared against a manually segmented image. Of course, the manually assessed threshold may not be the "best" one—which still remains unknown—but practically it makes sense to consider the manually thresholded image as a reference for the aim of this study. The automatic segmentation of each image is obtained by thresholding with the mean value of all the thresholds determined on each of the four VOI extracted from the original image. On the other hand, the manual binarization is realized by using a threshold proposed by an expert human supervisor. In both cases the post-processing step follows. The comparison is a simple strategy that allows to evaluate which one of the automatic thresholding techniques could be reasonably considered as the most

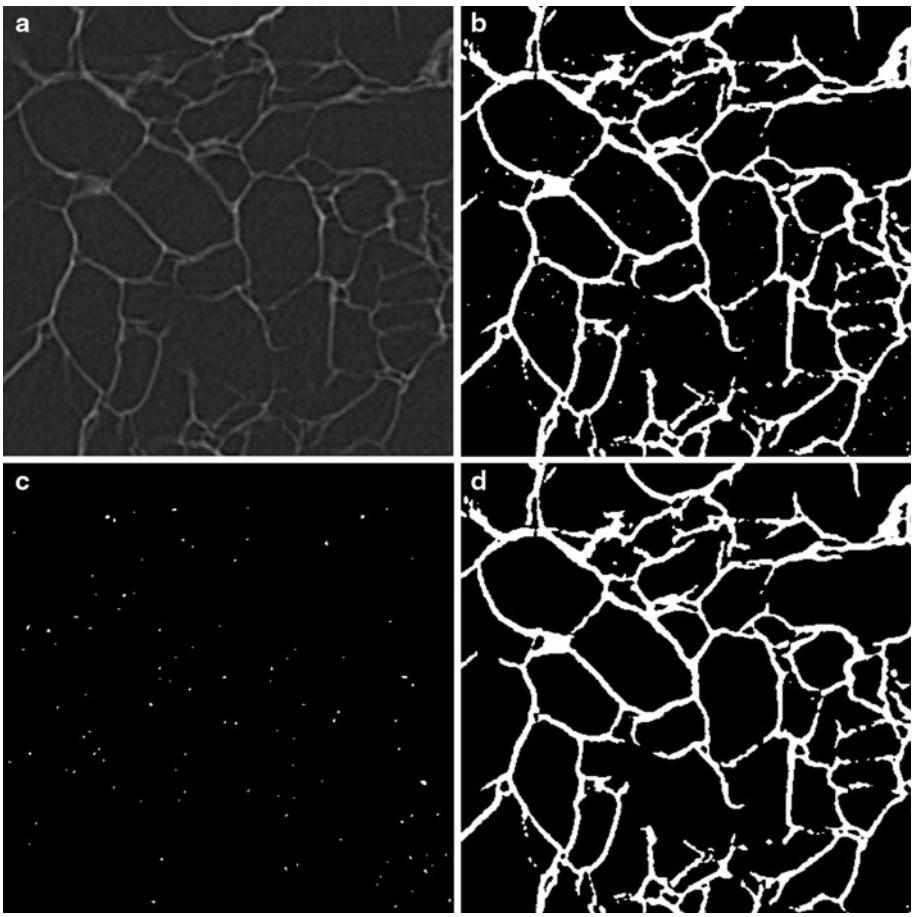

Fig. 2 Effects of the proposed post-processing on a slice of a VOI extracted from the CT dataset of the Alg/$CaCO_3$ sample: **a** original image; **b** simple thresholding (threshold determined according to the Kittler and Illingworth method); **c** elimination of all the connected components in touch with VOI margins resulting in an image with only binary noise; **d** difference of (**b**) minus (**c**) images, resulting in a correctly segmented image. For the sake of clarity only one slice of the VOI is shown though the processing is performed in 3D

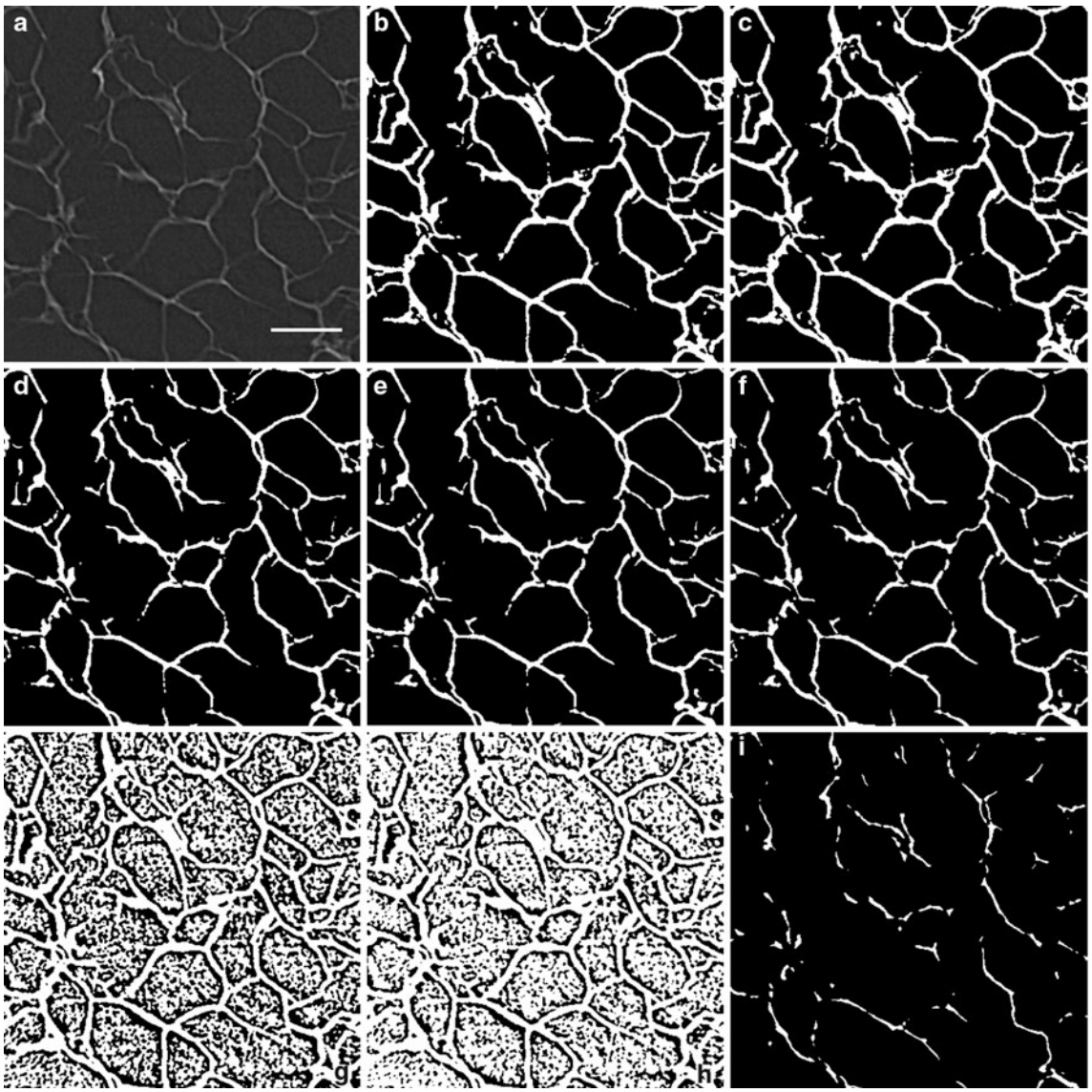

Fig. 3 Comparison of the different segmentation results (thresholding plus post-processing in all the cases): **a** original slice (the scale bar is 0.5 mm); **b** manual thresholding (threshold = 51); **c** Kittler's method (threshold = 50); **d** Ridler's method (threshold = 58); **e** Otsu's method (threshold = 59); **f** Tsai's method (threshold = 61); **g** Pun's method (threshold = 42); **h** Rajagopalan's method (threshold = 41); **i** Kapur's method (threshold = 81). For the sake of clarity only one central slice of the considered VOI of the Alg/$CaCO_3$ sample is shown, however 3D processing has been performed on the whole stack

effective at producing an image that is the most similar to the one proposed by an expert human supervisor. In the present paper the Misclassification Error (ME) [45] between the manually and the automatically segmented image is adopted. The ME is calculated as $1 - (TP + TN)/N$ where TP is the number of object voxels correctly detected (True Positives), TN is the number of background voxels correctly detected (True Negatives) and N is the total number of voxels. The misclassification error varies from 0, for a perfectly classified image, to 1 for a totally wrongly binarized image.

2.5 Basic characteristics

Starting from the correctly segmented VOI it is possible to compute several quantitative descriptors for the morphology of the considered scaffolds. In the present article, different families of descriptors are selected to be the most relevant to this aim. The first group represents basic characteristics: the volume density (V_V) or its complementary measure porosity ($1 - V_V$) and the specific surface area or surface density (S_V). These parameters are computed using the algorithms proposed in [33]. The

porosity represents the number of voxels belonging to the background with respect to the total number of voxels in VOI. The specific surface area is the interface area between the phases (the scaffold and the porous network) to the total volume of VOI ratio.

2.6 Structural anisotropy analysis

Information about the anisotropy of the microarchitecture is often necessary, i.e., the presence of preferential orientation(s) of the structure. The most commonly used method for the characterization of anisotropy is based on the mean intercept length (MIL) measure that computes the number of intersections between a linear grid and the pore/material interface as a function of the grid orientation [19]. Three dimensional MIL measurements may be then summarized by the isotropy index I that varies between 0 (all observation confined into a single plane or axis) and 1 (perfect isotropy) and the elongation index E that varies between 0 (no preferred orientation) and 1 (a perfect preferred orientation with only parallel observations).

2.7 Skeleton analysis

In the present paper, a family of descriptors based on *skeleton analysis* [23] is also proposed in order to derive pore and throat size distribution. In the present article the skeletonization algorithm presented in [2] has been adopted and pore and throat thickness measures were computed using the concept of maximal inscribed sphere [8] (see Fig. 4). However, the geometrical determination of pore and throat is difficult since there is no unambiguous geometrical definition of where a pore ends and a connecting channel begins. Conceptually, the skeleton nodes correspond to pore bodies and the branches of the pore space skeleton correspond to the channels (or paths) connecting the pores. However, a typical pore/node correction has to be applied since several skeleton nodes may occur in the same pore body [22, 24]. Some concerns still remain for the throats size determination. While very short branches are usually disregarded because some maximal balls centered at the skeleton nodes may completely include the short branches, incorrect channels may be still considered. Practically, this means that the throat size distribution may present some large-valued outliers due to the consideration of these branches that do not represent physical channels. Then, provided that the scaffold is a connected structure with no closed void cavities, a simple indicator of the connectedness of the 3D complex pore space is the Euler number χ_V. For an open network structure, the Euler number may be calculated from the number of nodes n and the number of branches b of the skeleton as $\chi_V = n - b$ [44]. It provides a measure of connectivity indicating the number of redundant connections. In order to normalize the Euler number with respect to the size of the considered volume V, the parameter *connectivity density* β computed as $\beta = (1 - \chi_V)/V$ is commonly adopted [31]. The connectivity density does not carry information about positions or size of connections but it is a simple global measure of connectivity which gives higher values for better-connected structures and lower values for poorly connected structures. In order to better characterize the connectivity, an interesting additional descriptor is the *coordination number* Z that represents the number of connections of a pore with its adjacent pores.

All the aforementioned analysis as well as the segmentation process have been carried out using the *Pore3D* software library [3]. Statistical analysis by means of the Wilcoxon signed rank test for the basic characteristics, the anisotropy analysis as well as the connectivity density and by means of the Wilcoxon rank sum test for pore size, throat size and coordination number was performed using *R* (www.r-project.org).

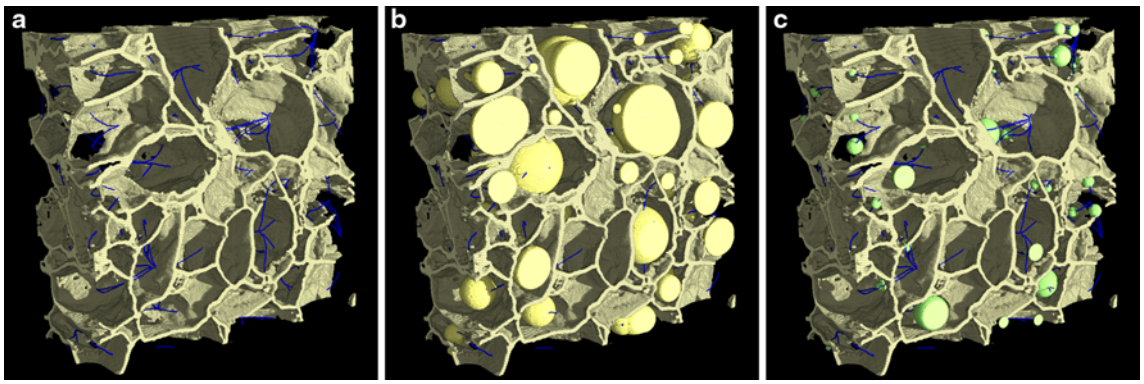

Fig. 4 Volume rendering (performed using the commercial software VG Studio MAX) of a portion of a considered VOI of the Alg/$CaCO_3$ sample: **a** rendering with skeleton of the porous network; **b** rendering which emphasizes some of the maximal balls used for the characterization of the pore size distribution; **c** rendering which emphasizes some of the maximal balls used for the characterization of the throat size distribution (Color figure can be viewed in the online edition)

3 Results and discussion

Table 1 reports threshold values for the manual assessment and for each automatic determination method considered in this study. Mean values and standard deviation of the threshold values were computed for all of the VOIs separately for each scaffold. The very low standard deviation values observed in the Pun's method and in the one proposed by Kittler and Illingworth indicate that they are insensitive to VOI selection. On the other hand, other methods (Huang and Wang, Kapur) exhibit high standard deviation suggesting a dependence from the region to which the VOIs belong. The latter methods have to be discarded because fluctuations in the threshold value affect further quantitative analysis.

Figure 3g shows that the threshold proposed by the Pun's method is too far from the manual one and also that the post-processing is not able to remove the binary noise introduced by the thresholding. This is confirmed in Table 2 in which the values of the misclassification error for each automatic thresholding method are reported. Moreover, since an automatic min/max normalization procedure was performed on each of the three μ-CT dataset, the three gray-level histograms are not comparable and it is worthy to notice that, for instance, the Otsu's method proposes the same threshold (59) for both the Alg/$CaCO_3$ and Alg/HApF samples while the Kittler and Illingworth method better adapts to the shifts in the image histogram suggesting a value closer to the manually selected one. Therefore, among the considered, the method proposed by Kittler and Illingworth is the most effective because it presents the lowest mean value of the misclassification error (about 1%) together with a very low dependence on the selected VOI.

Table 3 reports the quantitative results computed after the manual and the automatic segmentation with the Kittler and Illingworth method, respectively. It can be noticed that the differences in the segmentation affect the computation of parameters but in a negligible way and this is confirmed by the statistical analysis (Wilcoxon test) that revealed no *P*-value below the 0.05 significance level. With more details, in all the cases automatic segmentation provides threshold values lower than the manual ones. This means that the scaffold results slightly thicker in the case of the automatic segmentation producing lower values of porosity as well as higher values for specific surface area. Moreover, the differences observed for the basic characteristics in the case of the Alg/HApF sample are slightly greater than the ones observed for the other two samples which is consistent with the fact that the automatic proposed threshold is two gray-levels lower than the manual one (38 vs. 40) instead of just one gray-level found in the other cases (50 vs. 51 for the Alg/$CaCO_3$ sample and 52 vs. 53 for the Alg/nHAp sample).

On the other hand, the differences in the descriptors based on anisotropy and skeleton analysis are not affected

Table 1 Thresholds proposed by automatic methods for each considered VOI

	Kittler	Ridler	Otsu	Tsai	Pun	Rajagopalan	Kapur
Alg/$CaCO_3$ (manual threshold determination: 51)							
VOI_1	50	58	60	62	42	43	84
VOI_2	50	57	58	60	42	40	80
VOI_3	50	57	58	60	42	40	78
VOI_4	50	58	60	62	42	40	82
Mean	50	58	59	61	42	41	81
SD	0.000	0.500	1.000	1.000	0.000	1.299	2.236
Alg/nHAp (manual threshold determination: 53)							
VOI_1	52	64	66	72	46	46	108
VOI_2	52	67	68	75	46	46	108
VOI_3	52	65	66	73	46	46	112
VOI_4	52	64	65	71	46	46	108
Mean	52	65	66	73	46	46	109
SD	0.000	1.225	1.090	1.479	0.000	0.000	1.732
Alg/HApF (manual threshold determination: 40)							
VOI_1	38	56	57	64	30	28	83
VOI_2	38	56	58	65	30	29	90
VOI_3	38	58	59	66	30	29	79
VOI_4	38	58	60	67	30	28	77
Mean	38	57	59	66	30	29	82
SD	0.000	1.000	1.118	1.118	0.000	0.500	4.969

Mean values and standard deviation (*SD*) of the VOIs are also included for each method and for each considered sample

Table 2 Misclassification error for each considered automatic method and for each considered VOI with respect to the manual thresholding

Mean value of all the considered VOIs for all the samples is also reported

	Kittler	Ridler	Otsu	Tsai	Pun	Rajagopalan	Kapur
Alg/$CaCO_3$							
VOI_1	0.014	0.070	0.076	0.096	0.396	0.583	0.132
VOI_2	0.014	0.072	0.078	0.099	0.400	0.580	0.136
VOI_3	0.014	0.067	0.073	0.092	0.419	0.601	0.127
VOI_4	0.014	0.064	0.070	0.089	0.413	0.597	0.123
Alg/nHAp							
VOI_1	0.011	0.088	0.093	0.124	0.463	0.463	0.187
VOI_2	0.010	0.082	0.087	0.117	0.474	0.474	0.185
VOI_3	0.011	0.092	0.097	0.130	0.466	0.466	0.197
VOI_4	0.011	0.088	0.093	0.126	0.467	0.467	0.190
Alg/HApF							
VOI_1	0.008	0.045	0.051	0.062	0.415	0.515	0.132
VOI_2	0.008	0.047	0.053	0.065	0.404	0.502	0.141
VOI_3	0.007	0.044	0.050	0.061	0.397	0.496	0.137
VOI_4	0.007	0.043	0.049	0.059	0.409	0.506	0.130
Mean	0.011	0.067	0.073	0.093	0.427	0.521	0.151

Table 3 Comparison between the characterization of the considered samples adopting a manual segmentation (manual thresholding + post-processing) and the proposed automated segmentation (Kittler–Illingworth method + post-processing)

Mean value ± standard deviation among the considered Volumes of Interest (*VOI*) is reported except for pore size, throat size and coordination number. Mean value ± standard deviation of the total distribution of the considered pores is reported for pore size, throat size and coordination number

	Alg/$CaCO_3$	Alg/nHAp	Alg/HApF
Manual segmentation			
Basic characteristics			
Porosity ($1 - V_V$)	0.833 ± 0.003	0.808 ± 0.004	0.825 ± 0.004
Specific surface area (S_v) [mm^{-1}]	12.3 ± 0.4	10.5 ± 0.4	9.2 ± 0.3
Anisotropy analysis			
Isotropy index (I)	0.71 ± 0.02	0.62 ± 0.02	0.67 ± 0.03
Elongation index (E)	0.22 ± 0.01	0.33 ± 0.02	0.27 ± 0.03
Skeleton analysis			
Connectivity density [mm^{-3}]	15.5 ± 0.4	12.7 ± 1.8	15.0 ± 1.5
Coordination number (Z)	4.8 ± 3.1	4.7 ± 3.4	6.5 ± 7.0
Pore size [mm]	0.28 ± 0.12	0.31 ± 0.13	0.32 ± 0.15
Throat size [mm]	0.08 ± 0.05	0.08 ± 0.06	0.09 ± 0.06
Automated segmentation			
Basic characteristics			
Porosity ($1 - V_V$)	0.826 ± 0.003	0.797 ± 0.004	0.811 ± 0.004
Specific surface area (S_V) [mm^{-1}]	12.4 ± 0.4	10.8 ± 0.4	9.6 ± 0.3
Anisotropy analysis			
Isotropy index (I)	0.71 ± 0.01	0.67 ± 0.04	0.68 ± 0.03
Elongation index (E)	0.23 ± 0.01	0.28 ± 0.03	0.27 ± 0.01
Skeleton analysis			
Connectivity density [mm^{-3}]	14.4 ± 0.7	11.7 ± 1.5	14.6 ± 1.4
Coordination number (Z)	4.5 ± 2.7	4.7 ± 4.0	6.0 ± 5.2
Pore size [mm]	0.27 ± 0.11	0.30 ± 0.12	0.30 ± 0.13
Throat size [mm]	0.08 ± 0.05	0.08 ± 0.05	0.09 ± 0.06

by the slightly thicker scaffold obtained in the automatic segmentation case. In fact, the mean intercept length method for the computation of the isotropy and elongation indices is based on the number of intersections between a linear grid and the pore/material interface. Although slight variations in the threshold values influence the structure thickness, this fact does not directly imply variations in the pore/material interface. It is important to underline that, since the adopted implementation uses random orientations, minimal variations in the results are observed each

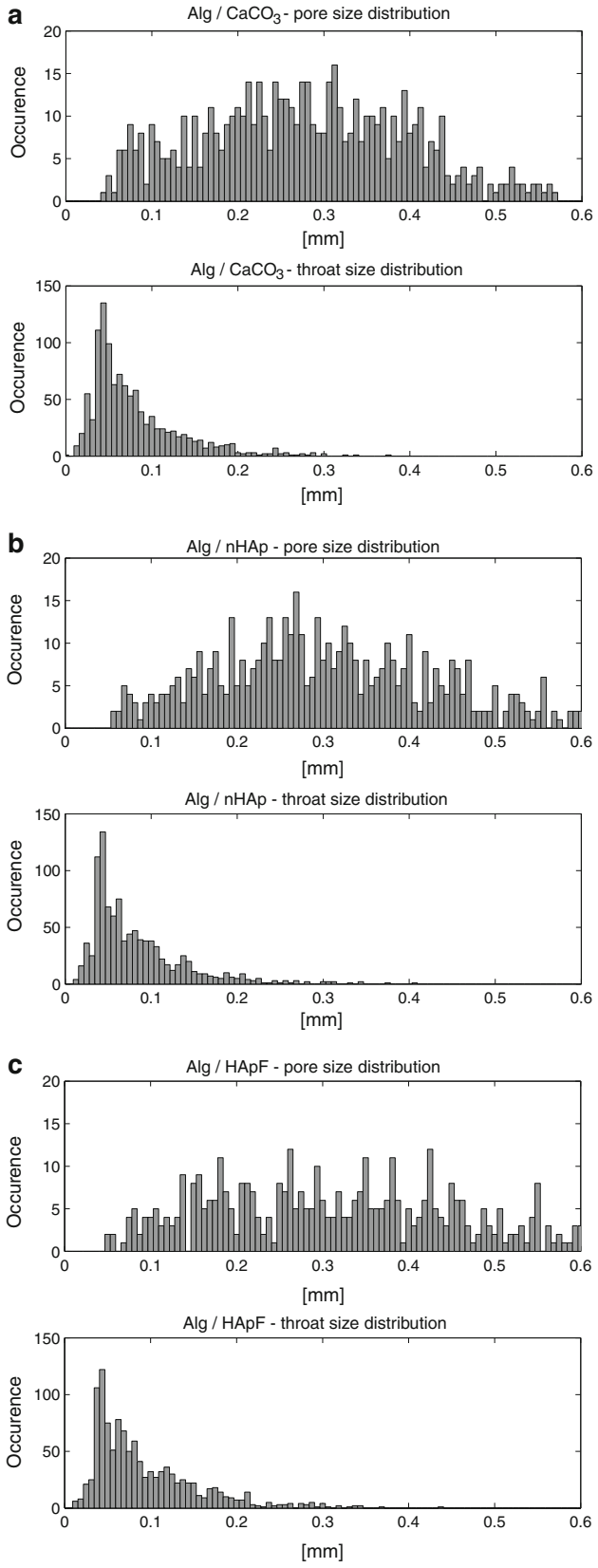

◀**Fig. 5** Distribution of pore and throat size for the considered samples in the case of the manual segmentation: **a** Alg/$CaCO_3$; **b** Alg/nHAp; **c** Alg/HApF. Each histogram is computed taking into account all the four VOIs and the size of the bins is equal to the voxel size of the images (6.25 μm)

time the code is executed. However, a simple test performed by re-computing 100 times the isotropy index I and the elongation index E on a single $2.5 \times 2.5 \times 2.5$ mm^3 (400^3 voxels) VOI revealed a coefficient of variation of about 0.007 for I and about 0.020 for E demonstrating that the random component in the computation of these parameters is not a concern. In the case of the Alg/$CaCO_3$ sample the isotropy index I is identical in both segmentations (0.71 ± 0.02 for the manual segmentation and 0.71 ± 0.01 for the automatic segmentation) while just slightly increasing values can be noticed for the Alg/nHAp sample (from 0.62 ± 0.02 for the manual segmentation to 0.67 ± 0.04 for the automatic segmentation) as well as for the Alg/HApF sample (from 0.67 ± 0.03 for the manual segmentation to 0.68 ± 0.03 for the automatic segmentation). In a similar way, the elongation index E increases for the Alg/$CaCO_3$ and Alg/nHAp samples while a minimal decrease may be observed for the Alg/HApF sample. It is reasonable to conclude that all samples present closely the same degree of anisotropy and that the slight variations in the segmentation threshold do not significantly affect the estimation of the isotropy and elongation indexes.

In the case of the automatic segmentation, the differences in the results of skeleton analysis are related to the increasing thickness of structures, which reduces the number of cavities in the scaffold's walls compared to the manually segmented case. A reduced number of branches and consequently a reduced number of nodes in the porous network are then identified by the skeleton analysis. However, due to the high number of nodes and branches considered, the pore and throat size distribution as well as the connectivity density and the coordination number are only marginally affected by these variations. Figures 5 and 6 present an almost identical behavior and, in addition, mean values (and standard deviation) for the pore and throat size distribution for all the considered samples present negligible differences.

The arbitrary selection of the μ-CT Volume of Interest (VOI) seems to not significantly affect the results since generally low standard deviations are observed. However, more accurate considerations that combine both size and position of the VOI are required. In fact, a low standard deviation may imply that a too small VOI was chosen and an insufficient number of elements was taken into account. An oversized volume would also result in minimal changes of the computed values when altering the VOI position as

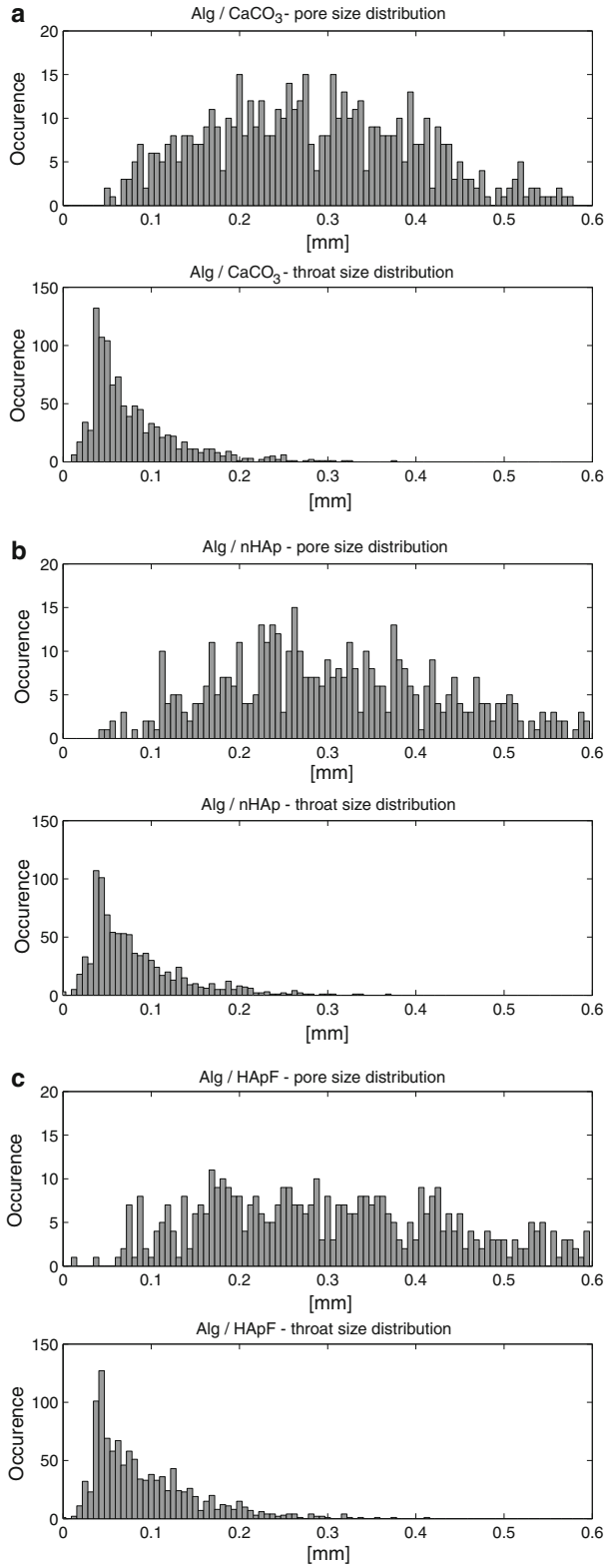

Fig. 6 Distribution of pore and throat size for the considered samples in the case of the automatic proposed segmentation: **a** Alg/$CaCO_3$; **b** Alg/nHAp **c** Alg/HApF. Each histogram is computed taking into account all the four VOIs and the size of the bins is equal to the voxel size of the images (6.25 μm)

the differences would simply average out. Figure 7 reports the results for the VOI representativeness check: for each parameter and for each sample, the mean value and the dispersion bar (±standard deviation) among the four VOIs cropped to the considered resize are reported. The sensitivity of each computed parameter with respect to the size of the VOI and, consequently, the representativeness of the considered VOI is suggested by the trend line among the different sizes and the dispersion bars. In general, a steady behaviour for both the trend line and the width of the dispersion bars suggests a proper VOI size. While, of course, this proper VOI size may differ among the parameters, generally the best trade-off is identified in order to assess all the parameters from the same VOIs. For the basic characteristics it can be noticed that even small VOIs may be used for the estimation of these parameters if the mean value of different VOIs is computed. A similar behaviour can be observed for the isotropy indices suggesting that the proposed 2.5^3 mm^3 VOI allows to get reliable results for the considered samples with respect to the adopted imaging resolution. On the other hand, the parameters based on skeleton analysis (pore and throat diameter, connectivity density and coordination number) require an adequate VOI size. In fact a more fluctuating trend for the small sizes can be noticed. This is because an insufficient number of nodes and branches are determined if small VOIs are considered. Keeping in mind that the mean pore size is around 300 μm and that only spheres totally incorporated into VOI margins are included in the computation of results, in a $0.6 \times 0.6 \times 0.6$ mm^3 (100^3 voxels) VOI a very low number of pores can be identified. Reliable results require an enlarged VOI and the $2.5 \times 2.5 \times 2.5$ mm^3 (400^3 voxels) VOI seems to be a good choice for the considered samples and the adopted imaging resolution. From a theoretical point of view, the adopted test for representativeness supposes that the investigated volume presents a micro-structural pattern repeated in some way throughout the sample and the test aims at identifying a VOI size that surely includes the pattern. Although such a perfectly repeated pattern cannot be theoretically supposed, the considered samples do present a regular architecture and therefore this test can supply useful information.

Focusing on the specific sample characteristics, it is allowed to conclude that the addition of hydroxyapatite (independently of average granule dimensions, at least in range from 120 to 150 nm) practically does not affect the overall characteristics of the freeze-casted alginate gels. Consequently, it appears that it is probably the combination of the 3D architecture of alginate gels together with the given procedure of freezing and sublimation which prevail in producing the final dry scaffold architecture. Further

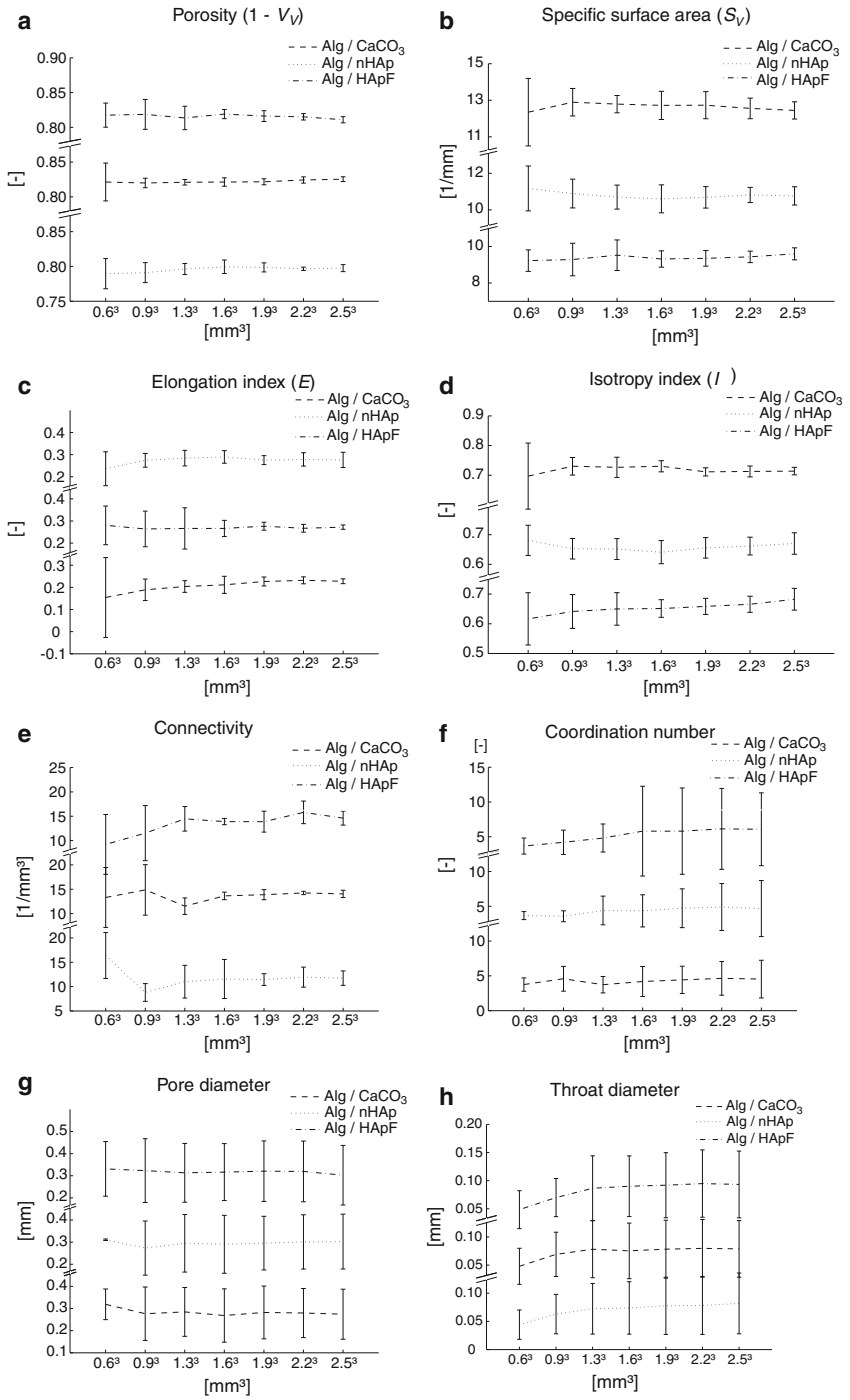

Fig. 7 Analysis of the representativeness of the proposed VOI size (only the case of automated segmentation is considered) for each quantitative descriptor: **a** porosity; **b** specific surface area; **c** elongation index; **d** isotropy index; **e** connectivity density; **f** coordination number; **g** pore diameter; **h** throat diameter. The average value with the dispersion bar (±standard deviation) of the four VOIs are reported for each cropped VOI size and for each considered sample

work using different polymeric gelling materials and freeze-casting procedure details is planned to assess the generality of this statement.

In bone biomaterial engineering, early studies showed that a minimum pore size of 100 μm was required to allow bone tissue ingrowth in ceramic scaffolds [13]. Further investigations were carried out to understand the structural requirements for bone tissue engineering. Although the optimal pore size vary with scaffold material, the general consensus is that an ideal scaffold should possess a global porosity in the range of 80–90% with interconnections of at least 50 μm in diameter between its macropores in the

100–400 μm pore size range [1, 17, 25, 28, 35]. The results of the micro-CT analysis show that the alginate/hydroxyapatite scaffolds analyzed in the present study have a suitable architecture for tissue engineering applications in terms of pore and throat size. Moreover, a quantification of the degree of anisotropy and interconnectivity confirm that alginate/hydroxyapatite biocomposite scaffolds for bone ingrowth are indeed trabecular structures with high and isotropic connectivity [43].

4 Conclusions

In the present article, a parameter-free and model-independent methodology for the characterization of bone tissue engineering scaffolds directly from computed microtomography (μ-CT) images is presented. An automatic segmentation method composed by the Kittler and Illingworth thresholding [20] and a parameter-free post processing cleaning step able to reduce misclassified voxels is proposed. After segmentation, the porosity as well as more refined descriptors such as pore and throat size, degree of interconnectivity and isotropy indices can then be computed. By analyzing μ-CT images of three different alginate/hydroxyapatite scaffolds it was here investigated how variations in the segmentation affect these numerical quantitative descriptors. Since the results showed negligible differences, it is here suggested that an automatic and objective segmentation has to be preferred. The proposed descriptors are also influenced by the selection of the volume of interest both in terms of position and dimensions. In the present study, it is suggested also how to correctly investigate on these crucial aspects. The resulting framework is an automatic tool for the characterization of bone tissue engineering scaffolds by means of μ-CT image analysis.

Acknowledgments The Authors gratefully acknowledge the access to the TOMOLAB μ-CT facility provided by SYRMEP group of the ELETTRA Synchrotron Radiation Facility in Basovizza, Trieste (Italy).

References

1. Bobyn JD, Pilliar RM, Cameron HU, Weatherly GC. The optimum pore size for the fixation of porous surfaced metal implants by the ingrowth of bone. Clin Orthop Relat Res. 1980;150:263–70.
2. Brun F, Dreossi D. Efficient curve-skeleton computation for the analysis of biomedical 3D images. Biomed Sci Instrum. 2010;46:475–80.
3. Brun F, Mancini L, Kasae P, Favretto S, Dreossi D, Tromba G. Pore3D: a software library for quantitative analysis of porous media. Nucl Instrum Methods Phys Res A. 2010;615:326–32.
4. Cartmell S, Huynh K, Lin A, Nagaraja S, Guldberg R. Quantitative microcomputed tomography analysis of mineralization within threedimensional scaffolds in vitro. J Biomed Mater Res A. 2010;69:97–104.
5. Darling A, Sun W. 3D microtomographic characterization of precision extruded poly-ε-caprolactone tissue scaffolds. J Biomed Mater Res A. 2004;70:311–7.
6. Elmoutaouakkil A, Fuchs G, Bergounhon P, Peres R, Peyrin F. Three-dimensional quantitative analysis of polymer foams from synchrotron radiation X-ray microtomography. J Phys D. 2003;2003:37–43.
7. Filmon R, Gaborit RN, Grizon F, Galloyer M, Cincu C, Basle MF, Chappard D. Non-connected versus interconnected macroporosity in poly(2-hydroxyethyl methacrylate) polymers. An X-ray microtomographic and histomorphometric study. J Biomater Sci Polym Ed. 2002;13:1105–17.
8. Hildebrand T, Rüegsegger P. A new method for the model-independent assessment of thickness in three-dimensional images. J Microsc. 1997;185:67–75.
9. Hilldore A, Wojtowicz A, Johnson AW. Micro-CT based quantification of non-mineralized tissue on cultured hydroxyapatite scaffolds. J Biomed Mater Res A. 2006;82:1012–21.
10. Hilldore A, Morgan AW, Woodard JR, Wagoner Johnson AJ. The curve integration method is comparable to manual segmentation for the analysis of bone/scaffold composites using micro-CT. J Biomed Mater Res B. 2009;88:271–9.
11. Ho ST, Hutmacher DW. A comparison of micro CT with other techniques used in the characterization of scaffolds. Biomaterials. 2006;27:1362–76.
12. Hollister SJ. Porous scaffold design for tissue engineering. Nat Mater. 2005;4:518–24.
13. Hulbert SF, Young FA, Mathews RS, Klawitter JJ, Talbert CD, Stelling FH. Potential of ceramic materials as permanently implantable skeletal prostheses. J Biomed Mater Res. 1970;4:433–56.
14. Itoh M, Shimazu A, Hirata I, Yoshida Y, Shintani H, Okazaki M. Characterization of CO_3Ap-collagen sponges using X-ray high-resolution microtomography. Biomaterials. 2004;25:2577–83.
15. Jones AC, Milthorpe B, Averdunk H, Limaye A, Senden TJ, Sakellariou A, Sheppard AP, Sok RM, Knackstedt MA, Brandwood A, Rohner D, Hutmacher DW. Analysis of 3D bone ingrowth into polymer scaffolds via micro-computed tomography imaging. Biomaterials. 2004;25:4947–54.
16. Kapur JN, Sahoo PK, Wong AKC. A new method for gray-level picture thresholding using the entropy of the histogram. Graph Models Image Process. 1985;29:273–85.
17. Karageorgiou V, Kaplan D. Porosity of 3D biomaterial scaffolds and osteogenesis. Biomaterials. 2005;26:5474–91.
18. Karande TS, Agrawal CM. Functions and requirements of synthetic scaffolds in tissue engineering. In: Laurencin C, Nair L, editors. Nanotechnology and tissue engineering: the scaffold. Broken Sound Parkway, NW: CRC Press; 2008. p. 53–86.
19. Ketcham RA, Ryan TM. Quantification and visualization of anisotropy in trabecular bon. J Microsc. 2004;213:158–71.
20. Kittler J, Illingworth J. Minimum error thresholding. Pattern Recogn. 1986;19:41–7.
21. Lin ASP, Barrows TH, Cartmell S, Guldberg R. Microarchitectural and mechanical characterization of oriented porous polymer scaffolds. Biomaterials. 2003;24:481–9.
22. Lindquist WB. Quantitative analysis of three dimensional X-ray tomographic images. Proc SPIE. 2002;4503:103–15.
23. Lindquist WB, Lee SM. Medial axis analysis of void structure in three-dimensional tomographic images of porous media. J Geophys Res. 1996;101:8297–310.
24. Lindquist B, Venkatarangan A. Investigating 3D geometry of porous media from high resolution images. Phys Chem Earth A. 1999;25:593–9.

25. Malafaya PB, Santos TC, van Griensven M, Reis RL. Morphology, mechanical characterization and in vivo neo-vascularization of chitosan particle aggregated scaffolds architectures. Biomaterials. 2008;29:3914–26.
26. Martin I, Mastrogiacomo M, De Leo G, Muraglia A, Beltrame F, Cancedda R, Quarto R. Fluorescence microscopy imaging of bone for automated histomorphometry. Tissue Eng. 2002;8:847–52.
27. Mastrogiacomo M, Komlev V, Hausard M, Peyrin F, Turquier F, Casari S, Cedola A, Rustichelli F, Cancedda R. Synchrotron radiation microtomography of bone engineered from bone marrow stromal cells. Tissue Eng. 2004;10:1767–74.
28. Mastrogiacomo M, Scaglione S, Martinetti R, Dolcini L, Beltrame F, Cancedda R. Role of scaffold internal structure on in vivo bone formation in macro-porous calcium phospate bioceramics. Biomaterials. 2006;27:3230–7.
29. Moore MJ, Jabbari E, Ritman EL, Lu L, Currier BL, Windebank AJ, Yaszemski MJ. Quantitative analysis of interconnectivity of porous biodegradable scaffolds with micro-computed tomography. J Biomed Mater Res A. 2004;71:258–67.
30. Murugan R, Ramakrishna S. Bioresorbable composite bone paste using polysaccharide based nano hydroxyapatite. Biomaterials. 2004;25:3829–35.
31. Odgaard A, Gundersen HJ. Quantification of connectivity in cancellous bone, with special emphasis on 3-D reconstructions. Bone. 1993;14:173–82.
32. Oh W, Lindquist B. Image thresholding by indicator kriging. IEEE Trans Pattern Anal Mach Intell. 1999;21:590–602.
33. Ohser J, Schladitz K. 3D images of materials structures: processing and analysis. Weinheim: Wiley-VCH; 2009.
34. Otsu N. A threshold selection method from gray-level histograms. IEEE Trans Syst Man Cybern. 1979;9:62–6.
35. Otsuki B, Takemoto M, Fujibayashi S, Neo M, Kokubo T, Nakamura T. Pore throat size and connectivity determine bone and tissue ingrowth into porous implants: three-dimensional micro-CT based structural analyses of porous bioactive titanium implants. Biomaterials. 2006;27:5892–900.
36. Peyrin F, Mastrogiacomo M, Cancedda R, Martinetti R. SEM and 3D synchrotron radiation micro-tomography in the study of bioceramic scaffolds for tissue-engineering applications. Biotechnol Bioeng. 2007;97:638–48.
37. Pun T. Entropic thresholding: a new approach. Comp Graph Image Process. 1981;16:210–39.
38. Rajagopalan S, Lu L, Yaszemski MJ, Robb RA. Optimal segmentation of microcomputed tomographic images of porous tissue-engineering scaffolds. J Biomed Mater Res A. 2005;75:877–87.
39. Ridler TW, Calvard S. Picture thresholding using an iterative selection method. IEEE Trans Syst Man Cybern. 1978;8:630–2.
40. Rosenfeld A, Kak AC. Digital picture processing. New York: Academic Press, Inc; 1982.
41. Sezgin M, Sankur B. Survey over image thresholding techniques and quantitative performance evaluation. J Electron Imag. 2004;13:146–65.
42. Tsai WH. Moment-preserving thresholding: a new approach. Graph Models Image Process. 1985;19:377–93.
43. Turco G, Marsich E, Bellomo F, Semeraro S, Donati I, Brun F, Grandolfo M, Accardo A, Paoletti S. Alginate/hydroxyapatite biocomposite for bone ingrowth: a trabecular structure with high and isotropic connectivity. Biomacromolecules. 2009;10:1575–83.
44. Whitehouse WJ. The quantitative morphology of anisotropic trabecular bone. J Microsc. 1974;101:153–68.
45. Yasnoff WA, Mui JK, Bacus JW. Error measures for scene segmentation. Pattern Recogn. 1977;9:217–31.
46. Zhang YJ. A survey on evaluation methods for image segmentation. Pattern Recogn. 1996;29:1335–46.